

Polyoxometalate-Based Metal–Organic Framework on Carbon Cloth with a Hot-Pressing Method for High-Performance Lithium-Ion Batteries

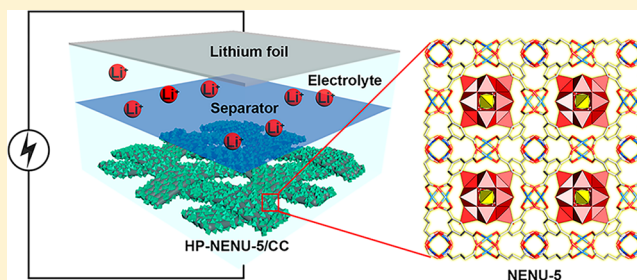
A-Man Zhang,[†] Mi Zhang,[†] Di Lan,[‡] Hai-Ning Wang,[†] Yu-Jia Tang,[†] Xiao-Li Wang,[†] Long-Zhang Dong,[†] Lei Zhang,[†] Shun-Li Li,^{*,†} and Ya-Qian Lan^{*,†}

[†]Jiangsu Collaborative Innovation Centre of Biomedical Functional Materials, Jiangsu Key Laboratory of New Power Batteries, School of Chemistry and Materials Science, Nanjing Normal University, Nanjing 210023, P. R. China

[‡]Faw Jilin Automobile Company, Ltd. (FAWMC), Jilin 132013, P. R. China

Supporting Information

ABSTRACT: Recently, development of a new type of anode material for lithium-ion batteries that possesses multielectron reaction, sufficient charge transfer, and restricted volume suppression has been considered a huge challenge. Herein, we find a simple hot-pressing method to incorporate polyoxometalate (POM)-based metal–organic frameworks (MOFs) onto three-dimensionally structured carbon cloth (CC), denoted as HP-NENU-5/CC, which immobilizes POMs into the MOFs avoiding the leaching of POMs and employs HP-NENU-5/CC as a flexible, conductive, and porous anode material. The HP-NENU-5/CC anode materials show outstanding electrochemical performance, exhibiting high reversible capacity (1723 mAh g^{−1} at 200 mA g^{−1}), high rate capability (1072 mAh g^{−1} at 1000 mA g^{−1}), and superior cycling stability (1072 mAh g^{−1} at 1000 mA g^{−1} after 400 cycles). Most importantly, the performance of HP-NENU-5/CC is the best among those of all reported POMs and MOF-based materials. In addition, we perform a comparative study for active materials coated on a two-dimensional current collector and CC, and our experimental results and analysis prove that the active material coated on CC does enhance the electrochemical performance.



INTRODUCTION

Along with the rapid growth of our economy and society, the demand for energy continues to grow. The problems of energy consumption and environmental pollution caused by burning fossil fuels are becoming more serious.^{1–3} Therefore, renewable energy and sustainable energy storage equipment are becoming the target of research worldwide for solving the energy and environmental crisis.⁴ Lithium-ion batteries (LIBs) have become the most important mobile storage technology.^{5–9} However, there is still a great challenge to improve the performance of LIBs, for example, by further improving the energy density, rate performance, and cycle life.

To deal with the problem, the employment of a high-performance electrode material is becoming a focus of research. Metal–organic frameworks (MOFs), known as a very promising kind of porous material, possess large surface areas, tunable pore volumes, and proper pore sizes. Because of these advantages, MOFs have been broadly applied in separation,¹⁰ sensors,¹¹ catalysis,¹² drug delivery,¹³ proton conduction,^{14–16} and energy storage.^{17–19} In particular, MOFs have been explored as either cathode or anode materials.^{1820–22} However, because of their limited reversible capacity or poor rate performance, MOF-based materials

cannot be used in practical applications. Naturally, these shortcomings of MOF-based LIBs still need to be resolved.

Simultaneously, polyoxometalates (POMs) generally possess redox properties, which have great potential applications for electrochemical energy storage^{23,24} and electrochemical catalysis.^{25–28} Awaie and co-workers have pioneered the use of phosphomolybdate as cathode materials, and the theoretical and experimental approach reveals that [PMo₁₂O₄₀]^{3−} (PMo₁₂) can act as an “electron sponge”, because of its high electron uptake number (24 electrons) between [PMo₁₂O₄₀]^{3−} and [PMo₁₂O₄₀].^{24,27} However, when POMs are explored for anode materials, they can be easily dissolved in the electrolyte, resulting in significant capacity degradation. To overcome this difficulty, POMs are usually combined with MOFs to fabricate polyoxometalate-based metal–organic frameworks (POMOFs). POMOFs combine the advantages of POMs and MOFs and are a perfect candidate for anode materials. To date, a series of POMOFs and POMOF-based materials, including POMOF-1, PMG-3, NUU-11, and NENU-507, have been used as anode materials for LIBs.^{29–32} The introduction

Received: July 5, 2018

Published: August 27, 2018

of POMs does improve the reversible capacity; however, the poor conductivity of the POMOFs results in a low cycling stability and a poor rate performance. Compared with the traditional two-dimensional (2D) current collector powdered materials, three-dimensionally structured carbon cloth (CC) has demonstrated the following advantages: special electron transfer, easy to obtain electrolyte, good strain adjustment, and sufficient spare volume. Therefore, it may be a good chance to prepare an electrode material based on POMOFs and CC with an extended cycle life and increase the rate capacity in a simple way.^{33–35}

Herein, by means of a hot-pressing method, NENU-5 is successfully located on the surface of CC (denoted as HP-NENU-5/CC), which is constructed from PMo_{12} , copper(II) acetate monohydrate $[\text{Cu}(\text{CH}_3\text{COO})_2 \cdot \text{H}_2\text{O}]$, and 1,3,5-benzenetricarboxylate (H_3BTC) and possesses kegglin-type POMs (PMo_{12}) in its pores compared with HKUST-1, and then we directly use them as integrated electrode materials for LIBs. The designed integrated electrode has the following advantages. (i) PMo_{12} as the “electron sponge” has 24 electrons that can be obtained for the best acceptance capability because of the formation of highly reduced transition species.²⁴ (ii) Immobilizing PMo_{12} into the MOF skeleton avoids dissolution in the electrolyte and enhances the electrochemical stability.³⁶ (iii) CC is used as a current collector in place of the 2D metal current collector (for example, copper or aluminum foil) because of the high mechanical strength and electrical conductivity and good corrosion resistance.³⁷ All in all, we observe the extraordinary electrochemical performance of the designed HP-NENU-5/CC electrodes. In detail, a high specific capacity of 1723 mAh g^{-1} after 100 cycles at a current density of 200 mA g^{-1} and a good rate capability are obtained. Furthermore, an excellent lifetime stability is obtained at a high rate of 1000 mA g^{-1} with a capacity retention of nearly 99.8% for 400 cycles.

EXPERIMENTAL SECTION

Synthesis of HP-NENU-5/CC. HP-NENU-5/CC was synthesized by a hot-pressing method. Briefly, H_3BTC (0.14 g), $\text{Cu}(\text{CH}_3\text{COO})_2 \cdot \text{H}_2\text{O}$ (0.20 g), PMo_{12} (0.17 g), and a certain amount of ethanol were placed in an agate mortar and then absolutely mixed by ball milling. Subsequently, the resulting slurries were coated on CC and heated with iron at 200°C for 20 min. Then the sample was successively washed with deionized water and absolute ethanol and dried at 90°C overnight. Similarly, HP-HKUST-1/CC and HP- PMo_{12} /CC were synthesized through the same method except that HP-HKUST-1/CC lacked PMo_{12} and HP- PMo_{12} /CC used only PMo_{12} .

Synthesis of Pre-NENU-5/CC. Pre-NENU-5/CC was synthesized through the same method with HP-NENU-5/CC except that NENU-5 was synthesized in advance³⁸ and then coated on CC through a hot-pressing method.

Synthesis of RGO/NENU-5. The electrode material of RGO/NENU-5 nanocomposites were prepared by our previous work.³⁸

Characterization of the Material. The phases of the as-synthesized samples were recorded as power X-ray diffraction (PXRD) patterns on a SmartLab 9KW Rigaku instrument equipped with graphite-monochromatized $\text{Cu K}\alpha$ radiation ($\lambda = 1.54060 \text{ \AA}$). The Fourier-transform infrared (FTIR) spectra were recorded with a Nexus 670 spectrometer. The morphology of the synthesized samples was collected on a scanning electron microscope (JEOL-2100F) and a transmission electron microscope on a JEM-200CX apparatus. The element distribution was characterized by elemental mapping and energy dispersive X-ray spectroscopy (EDX) with an X-Max-Vantage-type energy spectrometer (Oxford Instruments). X-ray photoelectron spectroscopy (XPS) measurements were taken on a scanning X-ray

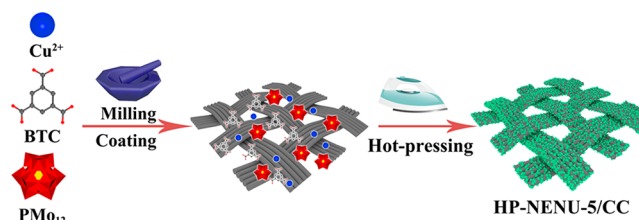
microprobe (K-Alpha, Thermo Scientific) with $\text{Al K}\alpha$ radiation and the C 1s peak at 284.6 eV as the internal standard.

Electrochemical Measurements. The preprocessed CC loaded with active materials (mass loading of $1.8\text{--}2.2 \text{ mg cm}^{-2}$) was directly employed as an integrated electrode for the work. Then the electrode was assembled into a cell with a CR2032-type coin cell in a glovebox filled with argon, and the water and oxygen content verged on 1 ppm. The cells consisted of pure lithium foil (the counter electrode), a separator (a Celgard 2400 microporous polypropylene membrane), an electrolyte [1 M LiPF_6 consisting of ethylene carbonate (EC) and dimethyl carbonate (DMC) with a volume ratio of 1:1], and active materials. The galvanostatic charge/discharge tests were performed on a LAND CT2001A (China) battery measurement system at different current densities with a cutoff voltage window of $0.01\text{--}3.0 \text{ V}$ versus Li^+/Li . Cyclic voltammetry (CV) and electrochemical impedance spectroscopy (EIS) curve studies were performed on an electrochemical workstation (CHI 660D). CV curves were measured at a scan rate of 0.02 mV s^{-1} over the voltage range of $0.01\text{--}3.0 \text{ V}$. EIS measurements were taken at an alternating current (ac) amplitude of 5.0 mV at different voltages with a frequency range from 100 kHz to 0.01 Hz .

RESULTS AND DISCUSSION

The schematic diagram for the detailed synthesis of HP-NENU-5/CC is illustrated in Scheme 1. First, PMo_{12} , Cu^{2+} ,

Scheme 1. Synthesis of HP-NENU-5/CC



and H_3BTC are milled uniformly in the mortar, giving NENU-5. Second, the as-formed NENU-5 microcrystals are coated on CC. Next, the integrated HP-NENU-5/CC electrodes are successfully prepared by a hot-pressing method. In a control experiment, we have synthesized HP-HKUST-1/CC and HP- PMo_{12} /CC in a manner similar to that used for HP-NENU-5/CC. The framework of HKUST-1, PMo_{12} , and NENU-5 is shown in Figure S1. The structure of NENU-5 is isostructural to that of HKUST-1, where PMo_{12} is immobilized in its pores. To address the effect of CC on the battery performance, NENU-5 and RGO/NENU-5 are also prepared for comparison. Pre-NENU-5/CC has been prepared to evaluate the influence of the in situ hot-pressing method on the performances of the LIBs.

The structures of as-prepared HP-NENU-5/CC (Figure 1a), HP-HKUST-1/CC, (Figure S2a), NENU-5, and RGO/NENU-5 (Figure S2b) are characterized by PXRD. As for HP-NENU-5/CC and HP-HKUST-1/CC, an obvious wide peak at $\sim 26.16^\circ$ belongs to CC. Clearly, all of these as-prepared samples match well with their simulated patterns, confirming the phase purity of these samples. The FTIR spectra of HP-NENU-5/CC, HP-HKUST-1/CC, and HP- PMo_{12} /CC are displayed in Figure 1b. The bands at 1714 and 1356 cm^{-1} in HP-HKUST-1/CC and HP-NENU-5/CC are ascribed to $\text{n}(\text{C}=\text{O})$ and $\text{n}(\text{C}-\text{O})$ from aromatic groups. With regard to the HP-NENU-5/CC and HP- PMo_{12} /CC samples, the characteristic bands located at 963 , 1055 , 778 , and 865 cm^{-1} are attributed to $\text{Mo}=\text{O}$, $\text{P}-\text{O}$, $\text{Mo}-\text{Oe}-\text{Mo}$, and $\text{Mo}-\text{Ob}-\text{Mo}$ stretching vibrations, respectively, which in-

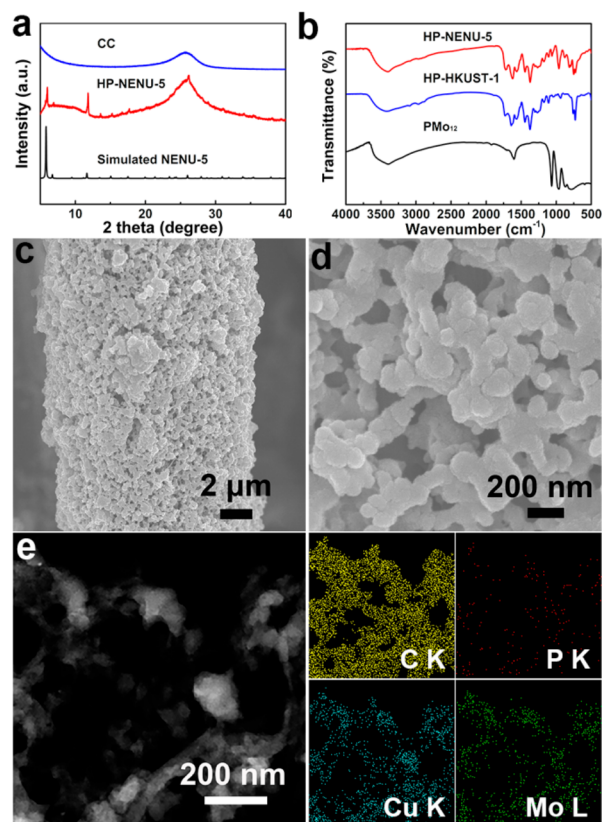


Figure 1. (a) PXRD patterns of simulated NENU-5 and HP-NENU-5/CC. (b) FTIR spectra of PMo₁₂/CC, HP-HKUST-1/CC, and HP-NENU-5/CC. (c and d) SEM images of HP-NENU-5/CC. (e) STEM image of HP-NENU-5/CC and mapping images of C, Cu, and P.

indicates that PMo₁₂ is successfully loaded into the frameworks of HKUST-1.

The scanning electron microscopy (SEM) image reveals that the morphology of bare CC is smooth, as shown in Figure S4a. After NENU-5 had been grown on CC by a hot-pressing method, the CC was uniformly covered with NENU-5 particles (Figure 1c,d). The transmission electron microscopy (TEM) image of HP-NENU-5/CC is displayed in Figure S3. As shown in panels c and d of Figure S4, HP-HKUST-1/CC also has a similar morphology. Similarly, the SEM and TEM images of HP-PMo₁₂/CC and pre-NENU-5/CC are shown in panels b, e, and f of Figure S4, indicating NENU-5 and PMo₁₂ were successfully loaded on CC. The detailed morphologies of NENU-5 and RGO/NENU-5 are shown in Figure S5. Figure 1e displays the scanning TEM (STEM) and EDX elemental mapping images for HP-NENU-5/CC. It demonstrates C, O, P, Mo, and Cu are uniformly distributed in HP-NENU-5/CC. In addition, as shown in Figure S6, the STEM and EDX elemental mapping images of HP-HKUST-1/CC show the uniform distribution of C, O, and Cu in HP-HKUST-1/CC.

XPS of HP-NENU-5/CC before and after discharge at 0.01 V has been performed to determine the compositions and element valences. As shown in panels a and b of Figure 2, the XPS survey spectra of the two samples show the existence of C, O, P, Cu, and Mo elements. The XPS spectrum of C 1s demonstrates three Gaussian peaks corresponding to C–C, C–O, and C=O, respectively (Figure 2c,d).^{30,39} As shown in Figure 2e, the two main peaks at 232.5 and 235.1 eV are associated with Mo⁶⁺ 3d_{5/2} and Mo⁶⁺ 3d_{3/2}, respectively.³⁹ In

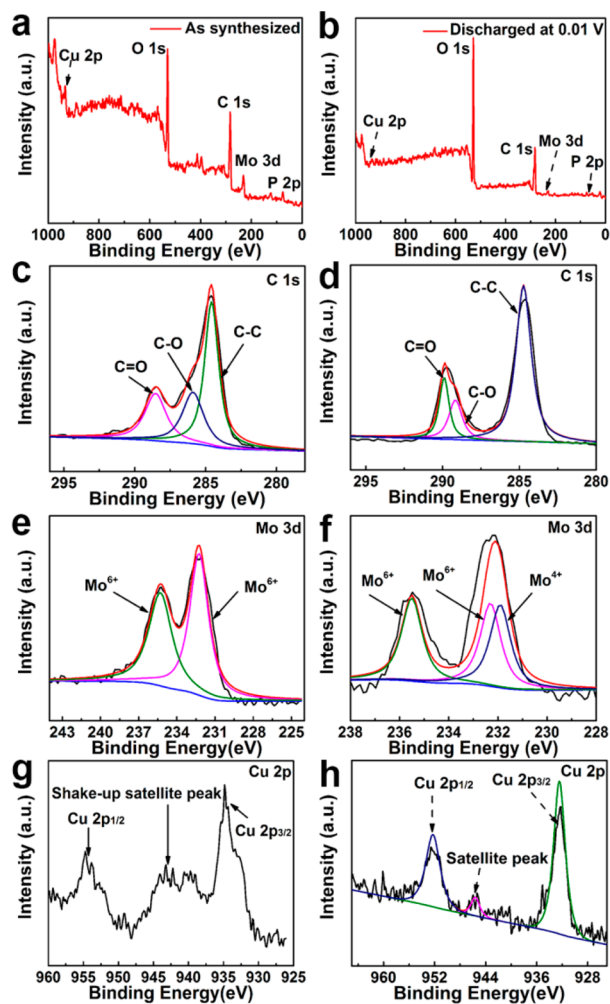


Figure 2. XPS spectra of HP-NENU-5/CC before and after discharging at 0.01 V. As-prepared samples: (a) survey scan, (c) C 1s, (e) Mo 3d, and (g) Cu 2p. Discharging at 0.01 V: (b) survey scan, (d) C 1s, (f) Mo 3d, and (h) Cu 2p.

addition, after discharging to 0.01 V has occurred, the Mo⁴⁺ peak appears at the position of 232.1 eV, which is ascribed to some Mo⁶⁺ being reduced to Mo⁴⁺, clearly seen in Figure 2f.⁴⁰ Furthermore, before discharging (Figure 2g), the Cu 2p spectrum has two main peaks of Cu 2p_{3/2} at binding of 934.9 eV and Cu 2p_{1/2} at binding of 954.9 eV as well as strong shakeup satellite peaks around 939.8 eV, and it can clearly prove the coexistence of Cu²⁺.⁴¹ After discharging to 0.01 V has occurred (Figure 2h), the peaks of Cu 2p_{3/2} and Cu 2p_{1/2} are located at 932.7 and 952.5 eV, still consistent with Cu²⁺.⁴¹ In addition, we also test the XPS of the as-prepared HP-HKUST-1/CC before and after discharge at 0.01 V in Figure S7; the XPS survey spectra of the samples show the existence of C, O, and Cu elements, and the valence of Cu exhibits no change (Figure S7c,f), which is consistent with the results for HP-NENU-5/CC.

The electrochemical performances of the as-synthesized electrodes, as LIBs anodes, was evaluated in lithium half-cells, which were cycled between 0.01 and 3.0 V versus Li⁺/Li. Figure 3a displays the 1st, 2nd, 10th, 50th, and 100th cycle charge–discharge profiles (galvanostatic) of the HP-NENU-5/CC electrode at a current density of 200 mA g^{−1}. Clearly, the first discharge profile varies from others because of the

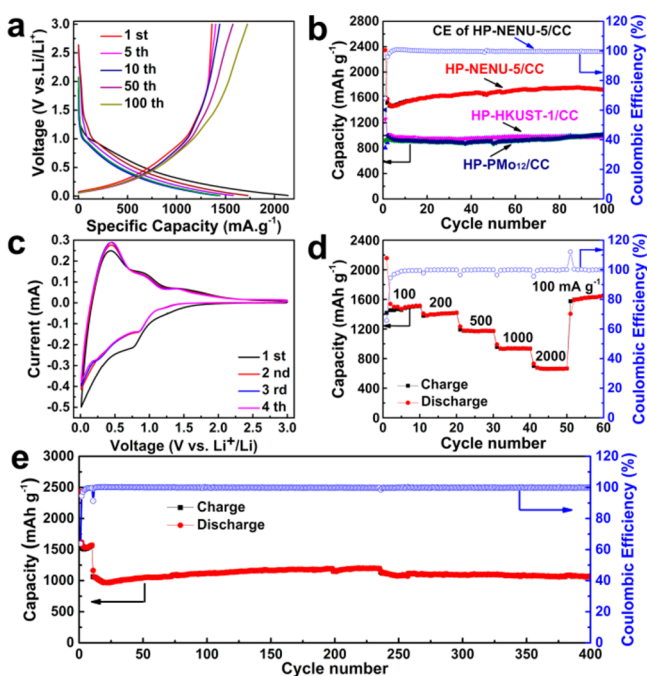


Figure 3. (a) Charge/discharge profiles of HP-NENU-5/CC after different cycles at 200 mA g^{-1} . (b) Cycling performance of HP-NENU-5/CC, HP-HKUST-1/CC, and HP-PMo₁₂/CC at a current density of 200 mA g^{-1} . (c) CV profiles of HP-NENU-5/CC at a scan rate of 0.2 mV s^{-1} . (d) Rate performance of HP-NENU-5/CC with several current densities from 100 to 2000 mA g^{-1} . (e) Stability test of HP-NENU-5/CC for 400 cycles at a current density of 1000 mA g^{-1} .

formation of the solid electrolyte interphase (SEI) membrane.^{42,43} From the second cycle onward, the similar shape and overlapped curves suggest the excellent reversibility of this material. The HP-NENU-5/CC electrodes deliver a high initial discharge capacity of approximately 2346 mAh g^{-1} and a charge capacity of 1595 mAh g^{-1} , much higher than those of HP-HKUST-1/CC (1259 and 805 mAh g^{-1} , respectively) and HP-PMo₁₂/CC (1147 and 1112 mAh g^{-1} , respectively) (Figures S11a and S12a), which results in a high first-cycle Coulombic efficiency (CE) of 68.1% .

Cycling performance is usually the main limitation for POMOFs. Figure 3b displays the comparative cycling stabilities and CE of the HP-NENU-5/CC, HP-HKUST-1/CC, and HP-PMo₁₂/CC electrodes that were determined at a current density of 200 mA g^{-1} for 100 cycles in the voltage range of $0.01\text{--}3.0 \text{ V}$. Apparent capacity deterioration is observed between the 1st and 5th cycles. While the capacity increases slightly over the cycle, the result may be attributed to the improved distribution of the electrolyte. After a few cycles, the CE of the HP-NENU-5/CC rapidly increased toward 99.8% , and for 100 cycles, the reversible capacities of the HP-NENU-5/CC, HP-HKUST-1/CC, and HP-PMo₁₂/CC electrodes are stabilized at around 1700 , 980 , and 1180 mAh g^{-1} , respectively. Clearly, HP-NENU-5/CC displays the highest capacity and excellent stability. Admittedly, the performance of pure CC has been reported previously,³⁷ and the results show that the contributions of pure CC to the total capacity can be negligible.

To identify the role of the in situ hot-pressing method, we also tested the cycling performance of Pre-NENU-5/CC at a current density of 200 mA g^{-1} (Figure S8). Pre-NENU-5/CC possesses first discharge and charge specific capacities of 2031

and 1138 mAh g^{-1} , respectively, lower than those of HP-NENU-5/CC, verifying the importance of the in situ hot-pressing method for the anode performance. In addition, to distinguish the current collector between three and two dimensions, we tested the cycling performance of NENU-5 on Cu foil with 70% active materials. As shown in Figure S9, the NENU-5 electrode displays a low reversible capacity of 201 mAh g^{-1} for 100 cycles. It is clear that the electrode materials grown on CC have a reversible capacity higher than the capacity of that coated on Cu foil. We also tested the performance of RGO/NENU-5 (Figure S10) at a current density of 1000 mA g^{-1} , and 300 cycles deliver a capacity retention of $\sim 600 \text{ mAh g}^{-1}$. Although the performances of the batteries of NENU-5 improve because of the effect of RGO, the performance of HP-NENU-5/CC is superior to that of RGO/NENU-5, which is due to the cooperation of stable NENU-5 microcrystals and the CC. Moreover, this cycling capacity is the highest among those of pristine MOFs, POMs, and POMOF-based and CC-based electrode materials previously reported (Table S1).

To investigate the electrochemical activity of HP-NENU-5/CC, CV measurements were performed with a scan rate of 0.2 mV s^{-1} over a voltage range of $0.01\text{--}3.0 \text{ V}$ for several cycles (Figure 3c). An irreversible peak at $\sim 0.6 \text{ V}$ appears during the first discharge, due to the formation of a SEI film, and then disappears during the following cycles.^{44,45} In the next scans, two visible peaks at potentials of 0.89 and 1.48 V belong to the oxidation process, and the strong peaks at 0.67 and 1.20 V appear during the reduction process, suggesting a precise electrochemical process. The result may be due to the redox property of the Mo and consistent with the XPS results in Figure 2f.³⁰

The rate performance is also an important parameter for assessing the batteries. Figure 3d shows the rate performance of HP-NENU-5/CC with current densities from 100 to 2000 mA g^{-1} , which exhibits a remarkable rate capability with high steady charge capacities of 1508 , 1418 , 1172 , 934 , and 662 mAh g^{-1} at 100 , 200 , 500 , 1000 , and 2000 mA g^{-1} , respectively. In particular, the capacity can maintain its original value when the current density returns to its initial rate after high-rate cycling. In comparison, the rate capacities of HP-HKUST-1/CC, HP-PMo₁₂/CC, Pre-NENU-5/CC, and RGO/NENU-5 are demonstrated in Figure S11b, S12b, S13b, and S14, respectively. The results demonstrate that HP-NENU-5/CC has the best rate performance. Furthermore, the HP-NENU-5/CC electrode also has an excellent performance at a high current density of 1000 mA g^{-1} as shown in Figure 3e. To activate the electrode, in the first 10 cycles, the current density was 100 mA g^{-1} . As a result, it can deliver a capacity of 1072 mAh g^{-1} for 400 cycles, demonstrating a superior stability and long lifetime. EIS characterization was also performed to further prove the advantage of HP-NENU-5/CC. HP-NENU-5/CC shows a charge transfer resistance after cycling that is lower than those of HP-HKUST-1/CC and HP-PMo₁₂/CC, as displayed in Figure S15.

To further investigate the electrochemical stability of HP-NENU-5/CC, we tested the PXRD of HP-NENU-5/CC after cycling (Figure S16). The result shows it maintains the original structure of NENU-5, demonstrating the excellent electrochemical stability of the electrode during discharging and charging. In addition, the SEM images of HP-NENU-5/CC before and after 100 cycles at a current density of 500 mA g^{-1} are also displayed in Figure S17, and the morphology does not

undergo an obvious change during the process, which indicates the stability of the electrode.

The excellent electrochemical performance of HP-NENU-5/CC might be due to the special structure. First, three-dimensional, flexible, and high-mechanical strength CC is used as a current collector in place of the traditional 2D metal current collector, improving the electronic conductivity of the electrode. Second, POMs are loaded into MOFs to construct POMOF materials, which not only reduces the rate of dissolution of POMs in the electrolyte but also enhances the electrochemical stability. Third, the NENU-5 directly grown on conductive flexible CC acts as an integrated electrode, successfully avoiding the use of a polymer binder, decreasing the size of the inactive interface, and also shortening the electron and ion transport path. Consequently, the HP-NENU-5/CC applied as the anode material delivers excellent cycling stability, significant rate capability, and a superior lifetime.

CONCLUSION

In summary, we successfully prepared the HP-POMOFs/CC electrodes through a hot-pressing method and employed them as anode materials for LIBs. The integrated HP-NENU-5/CC electrode is the best for lithium storage, which displays the largest capacity of 1723 mAh g⁻¹ at a current density of 200 mA g⁻¹ for 100 cycles. Importantly, nearly 99.8% of the capacity is retained at 1000 mA g⁻¹ for 400 cycles. It shows the outstanding electrochemical performances for lithium storage, which are attributed to the redox properties of POMs, the porous property of MOFs, and the excellent electronic conductivity of CC. This new strategy effectively improves the electrochemical performance by addressing the dissolution of POMs and the low electronic conductivity of MOFs, which can be applied in the new design for the development of MOFs, POMs, and POMOF-based materials for energy storage.

ASSOCIATED CONTENT

Supporting Information

The Supporting Information is available free of charge on the ACS Publications website at DOI: 10.1021/acs.inorgchem.8b01860.

Comparison of HP-NENU-5/CC with other pristine MOFs, POMs, and CC-based anodes, framework of the crystals, and characterization data from XRD, SEM, TEM, mapping, XPS, and other cycling performance (PDF)

AUTHOR INFORMATION

Corresponding Authors

*E-mail: yqlan@njnu.edu.cn.

*E-mail: slli@njnu.edu.cn.

ORCID

Long-Zhang Dong: 0000-0002-9276-5101

Ya-Qian Lan: 0000-0002-2140-7980

Author Contributions

A-M.Z. and M.Z. contributed equally to this work.

Notes

The authors declare no competing financial interest.

ACKNOWLEDGMENTS

This work was financially supported by the National Natural Science Foundation of China (21622104, 21471080, and 2170010097), the National Science Foundation of Jiangsu Province of China (SBK2017040708), the Natural Science Research of Jiangsu Higher Education Institutions of China (17KJB150025), the Priority Academic Program Development of Jiangsu Higher Education Institutions, and the Foundation of Jiangsu Collaborative Innovation Center of Biomedical Functional Materials.

REFERENCES

- (1) Jacobson, M. Z. Review of solutions to global warming, air pollution, and energy security. *Energy Environ. Sci.* **2009**, *2*, 148–173.
- (2) Xie, Z.; Xu, W.; Cui, X.; Wang, Y. Recent progress in metal-organic frameworks and their derived nanostructures for energy and environmental applications. *ChemSusChem* **2017**, *10*, 1645–1663.
- (3) Wang, L.; Han, Y.; Feng, X.; Zhou, J.; Qi, P.; Wang, B. Metal-organic frameworks for energy storage: Batteries and supercapacitors. *Coord. Chem. Rev.* **2016**, *307*, 361–381.
- (4) Liu, C.; Li, F.; Ma, L.-P.; Cheng, H.-M. Advanced materials for energy storage. *Adv. Mater.* **2010**, *22*, E28–E62.
- (5) Armand, M.; Tarascon, J. M. Building better batteries. *Nature* **2008**, *451*, 652.
- (6) Zhang, W.-M.; Hu, J.-S.; Guo, Y.-G.; Zheng, S.-F.; Zhong, L.-S.; Song, W.-G.; Wan, L.-J. Tin-nanoparticles encapsulated in elastic hollow carbon spheres for high-performance anode material in lithium-ion batteries. *Adv. Mater.* **2008**, *20*, 1160–1165.
- (7) Zhao, Y.; Li, X.; Yan, B.; Xiong, D.; Li, D.; Lawes, S.; Sun, X. Recent developments and understanding of novel mixed transition-metal oxides as anodes in lithium ion batteries. *Adv. Energy Mater.* **2016**, *6*, 1502175.
- (8) Xu, J.; Mahmood, J.; Dou, Y.; Dou, S.; Li, F.; Dai, L.; Baek, J.-B. 2D frameworks of C₂N and C₃N as new anode materials for lithium-ion batteries. *Adv. Mater.* **2017**, *29*, 1702007.
- (9) Goodenough, J. B.; Park, K.-S. The Li-ion rechargeable battery: A perspective. *J. Am. Chem. Soc.* **2013**, *135*, 1167–1176.
- (10) Dincă, M.; Long, J. R. Hydrogen storage in microporous metal-organic frameworks with exposed metal sites. *Angew. Chem., Int. Ed.* **2008**, *47*, 6766–6779.
- (11) Takashima, Y.; Martínez, V. M.; Furukawa, S.; Kondo, M.; Shimomura, S.; Uehara, H.; Nakahama, M.; Sugimoto, K.; Kitagawa, S. Molecular decoding using luminescence from an entangled porous framework. *Nat. Commun.* **2011**, *2*, 168.
- (12) Alkordi, M. H.; Liu, Y.; Larsen, R. W.; Eubank, J. F.; Eddaoudi, M. Zeolite-like metal-organic frameworks as platforms for applications: On metalloporphyrin-based catalysts. *J. Am. Chem. Soc.* **2008**, *130*, 12639–12641.
- (13) Horcajada, P.; Serre, C.; Vallet-Regí, M.; Sebban, M.; Taulelle, F.; Férey, G. Metal-organic frameworks as efficient materials for drug delivery. *Angew. Chem., Int. Ed.* **2006**, *45*, 5974–5978.
- (14) Kim, S.; Joarder, B.; Hurd, J. A.; Zhang, J.; Dawson, K. W.; Gelfand, B. S.; Wong, N. E.; Shimizu, G. K. H. Achieving superprotonic conduction in metal-organic frameworks through iterative design advances. *J. Am. Chem. Soc.* **2018**, *140*, 1077–1082.
- (15) Zhang, F.-M.; Dong, L.-Z.; Qin, J.-S.; Guan, W.; Liu, J.; Li, S.-L.; Lu, M.; Lan, Y.-Q.; Su, Z.-M.; Zhou, H.-C. Effect of imidazole arrangements on proton-conductivity in metal-organic frameworks. *J. Am. Chem. Soc.* **2017**, *139*, 6183–6189.
- (16) Li, X.-M.; Dong, L.-Z.; Li, S.-L.; Xu, G.; Liu, J.; Zhang, F.-M.; Lu, L.-S.; Lan, Y.-Q. Synergistic conductivity effect in a proton sources-coupled metal-organic framework. *ACS Energy Lett.* **2017**, *2*, 2313–2318.
- (17) Férey, G.; Millange, F.; Morcrette, M.; Serre, C.; Doublet, M.-L.; Grenèche, J.-M.; Tarascon, J.-M. Mixed-valence Li/Fe-based metal-organic frameworks with both reversible redox and sorption properties. *Angew. Chem., Int. Ed.* **2007**, *46*, 3259–3263.

- (18) Li, X.; Cheng, F.; Zhang, S.; Chen, J. Shape-controlled synthesis and lithium-storage study of metal-organic frameworks $\text{Zn}_4\text{O}(\text{1,3,5-benzenetribenzoate})_2$. *J. Power Sources* **2006**, *160*, 542–547.
- (19) Díaz, R.; Orcajo, M. G.; Botas, J. A.; Calleja, G.; Palma, J. Co8-MOF-5 as electrode for supercapacitors. *Mater. Lett.* **2012**, *68*, 126–128.
- (20) Liu, Q.; Yu, L.; Wang, Y.; Ji, Y.; Horvat, J.; Cheng, M.-L.; Jia, X.; Wang, G. Manganese-based layered coordination polymer: Synthesis, structural characterization, magnetic property, and electrochemical performance in lithium-ion batteries. *Inorg. Chem.* **2013**, *52*, 2817–2822.
- (21) Gou, L.; Hao, L.-M.; Shi, Y. X.; Ma, S.-L.; Fan, X.-Y.; Xu, L.; Li, D.-L.; Wang, K. One-pot synthesis of a metal-organic framework as an anode for Li-ion batteries with improved capacity and cycling stability. *J. Solid State Chem.* **2014**, *210*, 121–124.
- (22) Saravanan, K.; Nagarathinam, M.; Balaya, P.; Vittal, J. J. Lithium storage in a metal organic framework with diamondoid topology - a case study on metal formates. *J. Mater. Chem.* **2010**, *20*, 8329–8335.
- (23) Chen, J.-J.; Symes, M. D.; Fan, S.-C.; Zheng, M.-S.; Miras, H. N.; Dong, Q.-F.; Cronin, L. High-performance polyoxometalate-based cathode materials for rechargeable lithium-ion batteries. *Adv. Mater.* **2015**, *27*, 4649–4654.
- (24) Wang, H.; Hamanaka, S.; Nishimoto, Y.; Irle, S.; Yokoyama, T.; Yoshikawa, H.; Awaga, K. In operando X-ray absorption fine structure studies of polyoxometalate molecular cluster batteries: Polyoxometalates as electron sponges. *J. Am. Chem. Soc.* **2012**, *134*, 4918–4924.
- (25) Blasco-Ahicart, M.; Soriano-López, J.; Carbó, J. J.; Poblet, J. M.; Galan-Mascaros, J. R. Polyoxometalate electrocatalysts based on earth-abundant metals for efficient water oxidation in acidic media. *Nat. Chem.* **2017**, *10*, 24.
- (26) Yan, H.; Tian, C.; Sun, L.; Wang, B.; Wang, L.; Yin, J.; Wu, A.; Fu, H. Small-sized and high-dispersed WN from $[\text{SiO}_4(\text{W}_3\text{O}_9)_4]^{4-}$ clusters loading on GO-derived graphene as promising carriers for methanol electro-oxidation. *Energy Environ. Sci.* **2014**, *7*, 1939–1949.
- (27) Li, J.-S.; Wang, Y.; Liu, C.-H.; Li, S.-L.; Wang, Y.-G.; Dong, L.-Z.; Dai, Z.-H.; Li, Y.-F.; Lan, Y.-Q. Coupled molybdenum carbide and reduced graphene oxide electrocatalysts for efficient hydrogen evolution. *Nat. Commun.* **2016**, *7*, 11204.
- (28) Yan, H.; Tian, C.; Wang, L.; Wu, A.; Meng, M.; Zhao, L.; Fu, H. Phosphorus-Modified Tungsten Nitride/Reduced Graphene Oxide as a High-Performance, Non-noble-metal electrocatalyst for the hydrogen evolution reaction. *Angew. Chem., Int. Ed.* **2015**, *54*, 6325–6329.
- (29) Yue, Y.; Li, Y.; Bi, Z.; Veith, G. M.; Bridges, C. A.; Guo, B.; Chen, J.; Mullins, D. R.; Surwade, S. P.; Mahurin, S. M.; Liu, H.; Paranthaman, M. P.; Dai, S. A POM-organic framework anode for Li-ion battery. *J. Mater. Chem. A* **2015**, *3*, 22989–22995.
- (30) Wei, T.; Zhang, M.; Wu, P.; Tang, Y.-J.; Li, S.-L.; Shen, F.-C.; Wang, X.-L.; Zhou, X.-P.; Lan, Y.-Q. POM-based metal-organic framework/reduced graphene oxide nanocomposites with hybrid behavior of battery-supercapacitor for superior lithium storage. *Nano Energy* **2017**, *34*, 205–214.
- (31) Huang, Q.; Wei, T.; Zhang, M.; Dong, L.-Z.; Zhang, A. M.; Li, S.-L.; Liu, W.-J.; Liu, J.; Lan, Y.-Q. A highly stable polyoxometalate-based metal-organic framework with π - π stacking for enhancing lithium ion battery performance. *J. Mater. Chem. A* **2017**, *5*, 8477–8483.
- (32) Wang, Y.-Y.; Zhang, M.; Li, S.-L.; Zhang, S.-R.; Xie, W.; Qin, J.-S.; Su, Z.-M.; Lan, Y.-Q. Diamondoid-structured polymolybdate-based metal-organic frameworks as high-capacity anodes for lithium-ion batteries. *Chem. Commun.* **2017**, *53*, 5204–5207.
- (33) Zhang, G.; Hou, S.; Zhang, H.; Zeng, W.; Yan, F.; Li, C. C.; Duan, H. High-performance and ultra-stable lithium-ion batteries based on MOF-derived $\text{ZnO}@\text{ZnO}$ quantum dots/C core-shell nanorod arrays on a carbon cloth anode. *Adv. Mater.* **2015**, *27*, 2400–2405.
- (34) Xie, Q.; Zhang, Y.; Zhu, Y.; Fu, W.; Zhang, X.; Zhao, P.; Wu, S. Graphene enhanced anchoring of nanosized Co_3O_4 particles on carbon fiber cloth as free-standing anode for lithium-ion batteries with superior cycling stability. *Electrochim. Acta* **2017**, *247*, 125–131.
- (35) Wang, T.; Sun, C.; Yang, M.; Zhao, G.; Wang, S.; Ma, F.; Zhang, L.; Shao, Y.; Wu, Y.; Huang, B.; Hao, X. Phase-transformation engineering in MoS_2 on carbon cloth as flexible binder-free anode for enhancing lithium storage. *J. Alloys Compd.* **2017**, *716*, 112–118.
- (36) Ji, Y.; Hu, J.; Huang, L.; Chen, W.; Streb, C.; Song, Y.-F. Covalent attachment of anderson-type polyoxometalates to single-walled carbon nanotubes gives enhanced performance electrodes for lithium ion batteries. *Chem. - Eur. J.* **2015**, *21*, 6469–6474.
- (37) Balogun, M.-S.; Qiu, W.; Lyu, F.; Luo, Y.; Meng, H.; Li, J.; Mai, W.; Mai, L.; Tong, Y. All-flexible lithium ion battery based on thermally-etched porous carbon cloth anode and cathode. *Nano Energy* **2016**, *26*, 446–455.
- (38) Sun, C.-Y.; Liu, S.-X.; Liang, D.-D.; Shao, K.-Z.; Ren, Y.-H.; Su, Z.-M. Highly Stable Crystalline Catalysts Based on a Microporous Metal-Organic Framework and Polyoxometalates. *J. Am. Chem. Soc.* **2009**, *131*, 1883–1888.
- (39) Xie, J.; Zhang, Y.; Han, Y.; Li, C. High-Capacity Molecular Scale Conversion Anode Enabled by Hybridizing Cluster-Type Framework of High Loading with Amino-Functionalized Graphene. *ACS Nano* **2016**, *10*, 5304–5313.
- (40) Xia, F.; Hu, X.; Sun, Y.; Luo, W.; Huang, Y. Layer-by-layer assembled MoO_2 -graphene thin film as a high-capacity and binder-free anode for lithium-ion batteries. *Nanoscale* **2012**, *4*, 4707–4711.
- (41) Wang, C.; Zhu, J.; Liang, S.; Bi, H.; Han, Q.; Liu, X.; Wang, X. Reduced graphene oxide decorated with CuO - ZnO hetero-junctions: towards high selective gas-sensing property to acetone. *J. Mater. Chem. A* **2014**, *2*, 18635–18643.
- (42) Luo, L.; Wu, J.; Xu, J.; Dravid, V. P. Atomic resolution study of reversible conversion reaction in metal oxide electrodes for lithium-ion battery. *ACS Nano* **2014**, *8*, 11560–11566.
- (43) Su, Q.; Zhang, J.; Wu, Y.; Du, G. Revealing the electrochemical conversion mechanism of porous Co_3O_4 nanoplates in lithium ion battery by in situ transmission electron microscopy. *Nano Energy* **2014**, *9*, 264–272.
- (44) Bai, J.; Li, X.; Liu, G.; Qian, Y.; Xiong, S. Unusual formation of ZnCo_2O_4 3D hierarchical twin microspheres as a high-rate and ultralong-life lithium-ion battery anode material. *Adv. Funct. Mater.* **2014**, *24*, 3012–3020.
- (45) Reddy, M. V.; Subba Rao, G. V.; Chowdari, B. V. R. Metal oxides and oxysalts as anode materials for Li ion batteries. *Chem. Rev.* **2013**, *113*, 5364–5457.